PAPER • OPEN ACCESS

A minimal rupture cascade model for living cell plasticity

New Journal of Physics
The open access journal at the forefront of physics

Deutsche Physikalische Gesellschaft DPG
IOP Institute of Physics

Published in partnership with: Deutsche Physikalische Gesellschaft and the Institute of Physics

OPEN ACCESS

RECEIVED
21 March 2018

REVISED
26 April 2018

ACCEPTED FOR PUBLICATION
10 May 2018

PUBLISHED
29 May 2018

PAPER

A minimal rupture cascade model for living cell plasticity

Stefano Polizzi[1,2], **Bastien Laperrousaz**[3,4,5,6,7,8], **Francisco J Perez-Reche**[9], **Franck E Nicolini**[5,6,7,8], **Véronique Maguer Satta**[5,6], **Alain Arneodo**[1,2,4,6,10] **and Françoise Argoul**[1,2,4,6,10]

[1] CNRS UMR5798, Laboratoire Ondes et Matière d'Aquitaine, 351 cours de la Libération, F-33405 Talence, France
[2] Université de Bordeaux, Campus de Talence, 351 cours de la Libération, CS 10004, F-33405 Talence, France
[3] CEA Grenoble, BIOMICS-LBGE/ INSERM U1038, 17 avenue des Martyrs, F-38054 Grenoble, France
[4] UMR5672, Laboratoire de Physique, Ecole Normale Supérieure de Lyon, 46 Allée d'Italie, F-69007 Lyon, France
[5] CNRS UMR5286, INSERM U1052, Centre de Recherche en Cancérologie de Lyon, 28 rue Laennec, F-69008 Lyon, France
[6] Université de Lyon 1, 43 Boulevard du 11 Novembre 1918, F-69100 Villeurbanne, France
[7] Hematology Department, Centre Léon Bérard, 28 rue Laennec, F-69373 Lyon, France
[8] Hematology Department, Centre Hospitalier Lyon Sud, 165 Chemin du Grand Revoyet, F-69495 Pierre Bénite, France
[9] Institute for Complex Systems and Mathematical Biology, SUPA, University of Aberdeen AB24 3UE, United Kingdom
[10] Authors to whom any correspondence should be addressed.

E-mail: alain.arneodo@u-bordeaux.fr **and** francoise.argoul@u-bordeaux.fr

Keywords: nanoindentation AFM technique, cell mechanics, actin cytoskeleton, ductile and brittle failures, log-normal statistics, rupture cascade model, chronic myelogenous leukemia

Supplementary material for this article is available online

Abstract

Under physiological and pathological conditions, cells experience large forces and deformations that often exceed the linear viscoelastic regime. Here we drive $CD34^{+}$ cells isolated from healthy and leukemic bone marrows in the highly nonlinear elasto-plastic regime, by poking their perinuclear region with a sharp AFM cantilever tip. We use the wavelet transform mathematical microscope to identify singular events in the force-indentation curves induced by local rupture events in the cytoskeleton (CSK). We distinguish two types of rupture events, *brittle* failures likely corresponding to irreversible ruptures in a stiff and highly cross-linked CSK and *ductile* failures resulting from dynamic cross-linker unbindings during plastic deformation without loss of CSK integrity. We propose a stochastic multiplicative cascade model of mechanical ruptures that reproduces quantitatively the experimental distributions of the energy released during these events, and provides some mathematical and mechanistic understanding of the robustness of the log-normal statistics observed in both brittle and ductile situations. We also show that brittle failures are relatively more prominent in leukemia than in healthy cells suggesting their greater fragility.

1. Introduction

As the elementary building block of living systems, cells are active mechanical machines that constantly remodel their structural organization to withstand forces and deformations and to promptly adapt to their mechanical environment [1, 2]. This versatility is fundamentally required for many vital cellular functions, and an alteration of the cell mechanical properties can participate in pathogenesis and disease progression [3, 4]. Identifying under which conditions is the mechanical resilience of living cells compromised is therefore a critical issue. Significant progress in the past decades has provided a rather complete picture of the linear mechanical response to small applied stresses or strains [5–11]. However, cells are often subject to large deformations and reach nonlinear regimes that are far from being well understood [8, 9, 12–14]. The fascinating mechanical properties of living cells are mediated by the cytoskeleton (CSK), a dynamic network of filamentous proteins composed of actin filaments, microtubules, and intermediate filaments [7–9, 15–17]. The actin filaments are cross-linked by a wide variety of actin binding proteins (ABPs) [7–9, 12, 15–18]. By tuning the proportions of passive and active ABPs, living cells can control their power-law (scale-free) CSK rheology [7, 19]. Interestingly, cells exhibit both solid and liquid-like properties. Solid-like behavior is associated with strongly cross-linked actin filaments which

resist sliding and accumulate tension (fimbrin and fascin are compact cross-linking proteins that create parallel-aligned actin networks (actin bundles) and are found in stiffer membrane protusions of filopodia [20, 21]). In contrast, weakly cross-linking proteins produce actin filaments which slide more readily, enabling the network to flow as a liquid (α-actinin and filamin-A are less compact and form networks with more widely spaced and orthogonally aligned actin filaments[22]). All these actin cross-linking and/or bundling proteins work cooperatively or competitively, for instance fascin and α-actinin were recently shown to segregate into discrete bundled domains that are specifically recognized by other ABPs [23]. Under nonlinear loading conditions, living cells can display apparently opposite behaviors ranging from stress stiffening mainly governed by filament and/or cross-linker nonlinear elasticity [8, 9, 12, 13], to stretch softening and fluidization likely due to force-induced unbinding of ABPs [8, 9, 14]. This paradox can be solved by considering that, upon large deformations, the CSK of a living cell can undergo deep structural transformations such as the unfolding of protein domains, the unbinding of cytoskeletal cross-linkers, and the breaking of weak sacrificial bonds. All these structural changes are inelastic (non-reversible in a strict sense), they dissipate locally the elastic energy of the CSK network (structural damping) [24, 25]. Unbinding events and bond breakings confer living cells with the unique ability to adapt to different mechanical situations by actively controlling the amount of stress stiffening and fluidization [24, 26]. At the same time, such events reduce the connectivity of the CSK and may result in permanent plastic deformations or even more dramatic irreversible failures [8, 9] which, for instance, could be at the origin of the recently observed incomplete shape recovery of living cells after repeated creep [27]. These effects are reminiscent of those in cyclically loaded solids which can lead to fatigue-induced failure [28–30].

In this paper, we use a nanoindentation (AFM) technique [31–35] to experimentally investigate the nonlinear mechanical plasticity of single immature $CD34^+$ hematopoietic cells from healthy donors and patients suffering from chronic myelogenous leukemia (CML) in chronic phase (CP) harvested at diagnosis [36]. Classical analysis of force-indentation curves (FICs) aims at estimating an elastic modulus by fitting the curves with linear elastic models [37, 38]. Here, in contrast, we engineer a wavelet-based multi-scale method [36, 39] to identify singularities in the FICs that likely correspond to rupture events in the CSK. Our study provides compelling evidence of the existence of two distinct populations of avalanche rupture events, that we identify to *ductile* (corresponding to weakly cross-linked filaments) and *brittle* (corresponding to tightly cross-linked filaments) failures. Both mechanisms display fat-tail distributions of released energy well approximated by log-normal distributions. This is surprising given the ubiquity of power-law statistics for avalanches in solids [28–30]. We develop a minimal model that reproduces quantitatively the experimental released energy distributions, and provides some mechanistic interpretation of both the ductile and brittle rupture regimes. Despite this phenomenological model does not take into account the visco-elasticity of individual polymer chains constituting the CSK filaments, it sheds a new light on the local unbinding events as a major mechanism underlying the nonlinear response of living cells to large deformations and it further shows that brittle failures are more frequent in CML cells as the signature of their higher mechanical fragility.

2. Results

2.1. Nanoindentation of living hematopoietic primary cells

CML arises from a hematopoietic stem cell transformation following the formation of the BCR-ABL oncogene by a single reciprocal chromosomal translocation $t(9;22)$ [40]. In CML, $BCR\text{-}ABL^+$ cells of the myeloid lineage proliferate uncontrollably, the bone marrow density increases considerably, and their mechanical properties change during disease progression [41]. In transformed cells [42], BCR-ABL was shown to bind actin filaments, to inhibit their polymerization and to disorganize the CSK into punctuate, juxtanuclear aggregates [43–45]. We used AFM to indent single hematopoietic purified $CD34^+$ cells from CP-CML patients at diagnosis and healthy donor bone marrows [36] (see appendix A). We indented the cells by moving vertically the AFM cantilever (figure 1(a)) toward their perinuclear central region (figure 1(b)), at constant speed $V_0 = 1\ \mu\text{m s}^{-1}$ until a cantilever set-point force was reached. Then the cantilever was withdrawn from the sample at the same constant speed ($-V_0$) back to its starting position (figures 1(c) and (d)). From these indentation experiments, the cell shear relaxation modulus $G(Z)$ was estimated as the second-order derivative of the FIC (see equation (B13) in appendix B) [36, 39]. From the approach and retract FICs, the initial G_i and global G_g shear moduli, and the dissipation loss D_l were retrieved (see figure S1 is available online at stacks.iop.org/NJP/20/053057/mmedia and supplemental material[11]). When these FICs do not superimpose (figures 1(c) and (d)), D_l quantifies the percentage of work not restituted during retract and dissipated partly as viscous loss [31, 36]. Interestingly, the experimental FICs display fluctuations that locally exceed the background thermal fluctuations of the AFM cantilever [36] (figures 1(c) and (d)). We developed a wavelet-based detection method of these singular events

[11] See supplemental material for the estimation of global mechanical parameters from FICs and 15 additional figures.

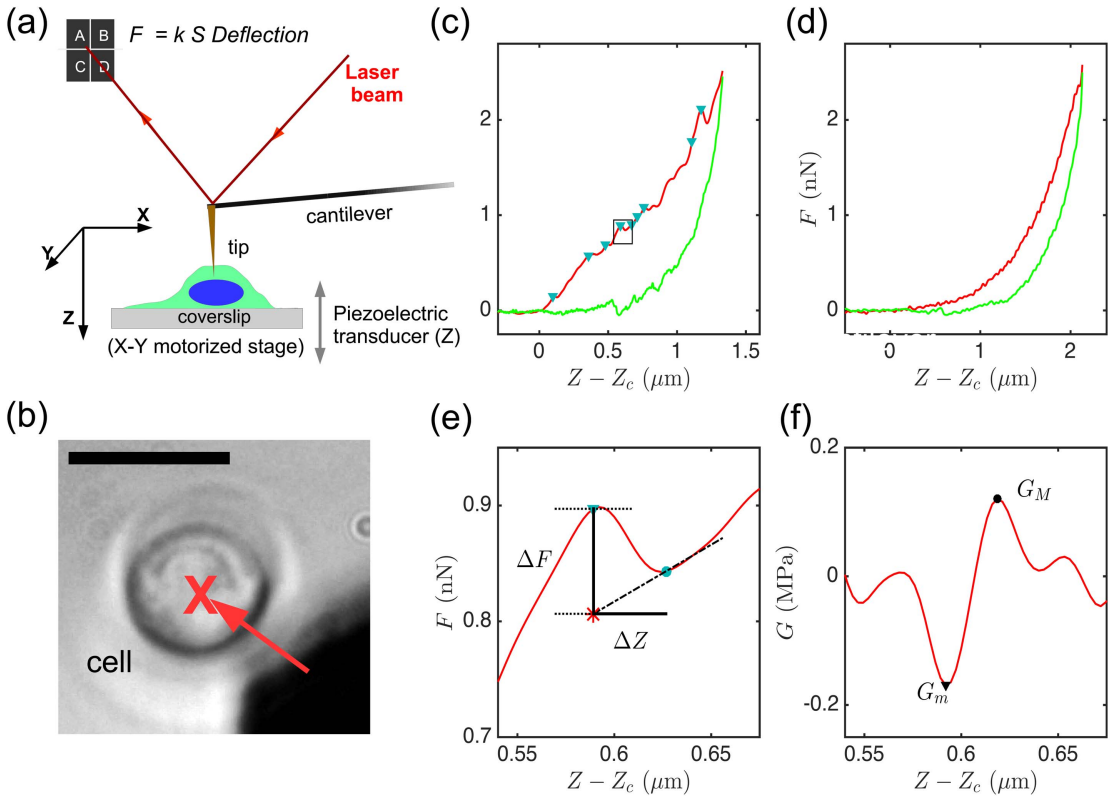

Figure 1. Principle of living cell indentation and detection of rupture events with an AFM cantilever tip. (a) Sketch of the AFM set up. (b) Microscopy transmission image of the perinuclear central region of an hematopoietic cell probed by the cantilever tip. Scale bar: 10 μm. (c) Typical approach (red) and retract (green) FICs collected on a CML hematopoietic cell (CP-CML patient). (d) Same as (c) but for a normal hematopoietic cell (healthy donor). (e) Zoom on (c) around a disruption event. (f) Corresponding second-order derivative $G(Z)$ of the FIC (see equation (B13) in appendix B) computed with a wavelet of size $w = 2\sqrt{2}s = 42$ nm; the local minima G_m (resp. maxima G_M) of d^2F/dZ^2 corresponding to a strong negative (resp. positive) curvature of the FIC are marked with black triangles (resp. dots). In a close neighborhood of G_m and G_M, the local maxima and minima of the FIC are detected and marked with blue triangles and dots in (c) and (e). The force drop ΔF of a disruption event is corrected by taking into account the increasing behavior of the FIC (linear dashed–dotted line in (e)).

that amounts to detect local curvature minima G_m and maxima G_M in the FICs (figures 1(e) and (f)) (see also appendix B, and figures S2 and S3 (see footnote 11)). For each disruption event, we computed the force drop ΔF, the penetration length ΔZ, and the released energy $E = \Delta F.\Delta Z$ (figure 1(e)). FICs without disruption events were not included in the statistics.

2.2. Ductile versus brittle rupture events

We collected two large sets of single cell FICs from 5 CP-CML patients (1301 FICs—49 cells) and 5 healthy donors (1671 FICs—60 cells). We detected 6161 singular rupture events distributed on 1153 FICs in CP-CML cells as compared to 6765 rupture events distributed on 1111 FICs in normal cells. Thus only 11.4% (148/1301) of FICs do not display rupture events for CML cells which is significantly lower than 33.5% (560/1671) for normal cells. The computation of the normalized histograms (p.d.f. for probability density function) of ΔZ, ΔF, and E of these rupture events, revealed rather wide distributions with fat-tail (see figure S4 (see footnote 11)). When focusing on ΔZ (nm), which can also be interpreted as the time duration $\Delta t = \Delta Z/V_0$ (ms) of the rupture event, we got very satisfactory fits of the p.d.f. of $\log_{10}(\Delta Z)$ with the sum of two distinct Gaussian distributions (see equation (B14) in appendix B) for both normal and CML cells (figures 2(a) and (b)). Thus, we identified two populations of rupture events, a subpopulation 1 of rather short duration ($\overline{\Delta t_1} \sim 30$ ms) and weakly penetrating ($\overline{\Delta Z_1} \sim 30$ nm) failures, and a subpopulation 2 of longer ($\overline{\Delta t_2} \sim 50$ ms) and deeply penetrating ($\overline{\Delta Z_2} \sim 50$ nm) failures. But what distinguishes CML from normal cells is the higher percentage ($\alpha = 0.34$ compared to 0.26) of the larger rupture events (subpopulation 2) in the CP-CML cells, as an indication of their greater mechanical brittleness.

When investigating the correlations between ΔZ, ΔF and E, we found a rather strong correlation between $\log_{10}(\Delta F)$ and $\log_{10}(\Delta Z)$ for both the CML (Pearson's correlation coefficient $r = 0.68$) and the normal ($r = 0.62$) cells. $\text{Log}_{10}(E)$ and $\log_{10}(\Delta Z)$ were also found significantly correlated in CML ($r = 0.83$) and in normal ($r = 0.80$) cells. These correlations issue from the existence of two clouds of points in the respective scatter plots (figures 2(c) and (d)), corresponding to subpopulation 1 of small indentation depth, short duration,

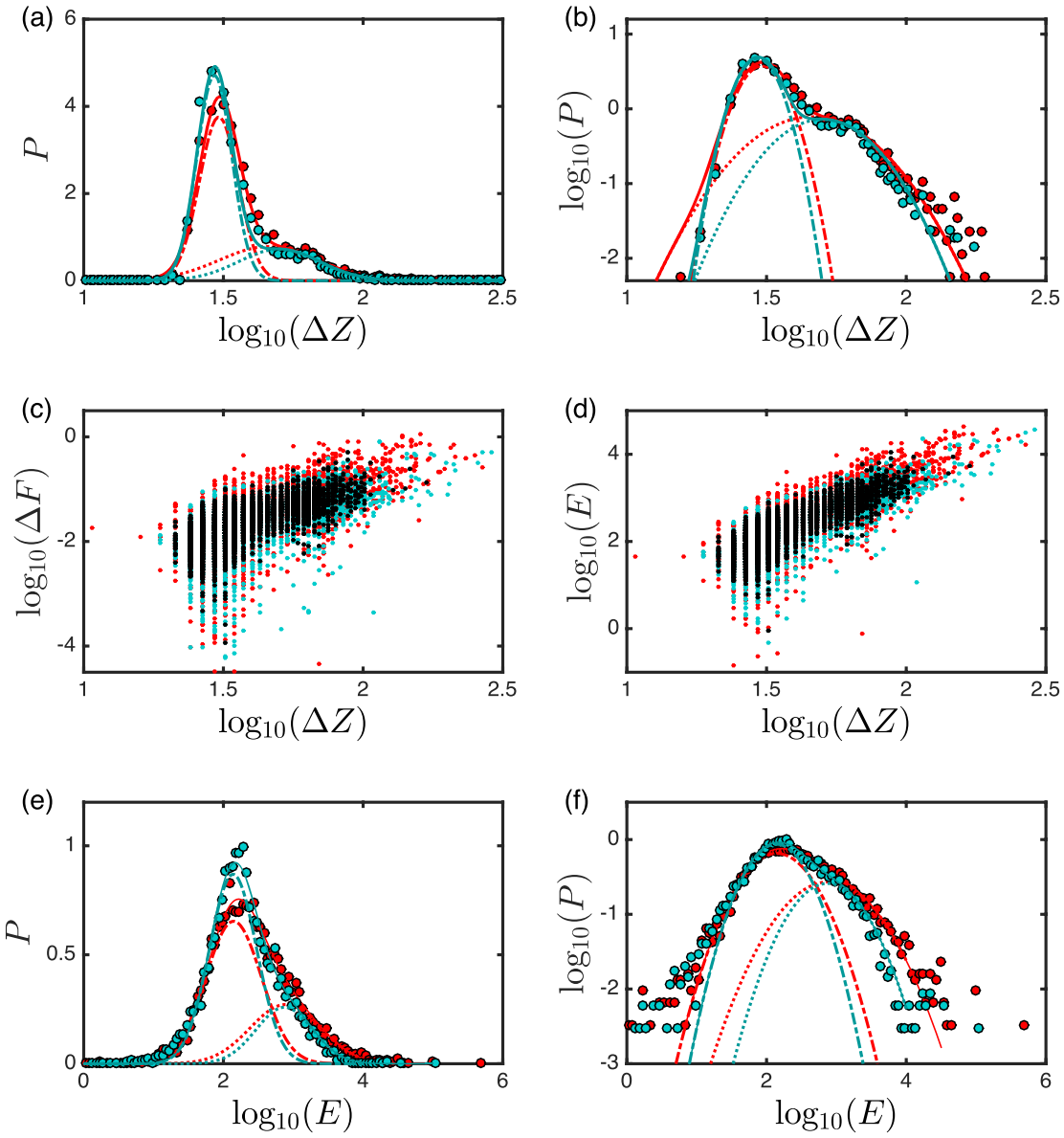

Figure 2. Statistical analysis of the indentation depths (nm), force drops (nN) and released energies (k_BT) of disruption events. These parameters were obtained from local disruption events collected from the FICs of the two sets of CML (red) and normal (blue) cells. (a) Normalized histograms of $\log_{10}(\Delta Z)$; the dots represent the experimental data and the continuous lines the corresponding fits by the sum of 2 Gaussian distributions (see equation (B14) in appendix B) with parameters $\alpha = 0.34$, and $\mu_1 = 1.49, \sigma_1 = 0.07$ corresponding to the following means $\overline{\Delta Z_1} = 31$ nm and $\widetilde{\Delta Z_1} = 31$ nm (red dotted–dashed line), $\mu_2 = 1.67, \sigma_2 = 0.18$, i.e., $\overline{\Delta Z_2} = 51$ nm and $\widetilde{\Delta Z_2} = 47$ nm (red dotted line) for CML cells, and $\alpha = 0.26$, and $\mu_1 = 1.47, \sigma_1 = 0.06$, i.e., $\overline{\Delta Z_1} = 30$ nm and $\widetilde{\Delta Z_1} = 29$ nm (blue dotted–dashed line), $\mu_2 = 1.70, \sigma_2 = 0.15$, i.e., $\overline{\Delta Z_2} = 53$ nm, and $\widetilde{\Delta Z_2} = 50$ nm (blue dotted line) for normal cells. (b) Same as (a) but in a logarithmic representation where Gaussians become parabolae. (c) Scatter plot of $\log_{10}(\Delta F)$ versus $\log_{10}(\Delta Z)$; each red (resp. blue) dot corresponds to a rupture event in a CML (resp. normal) FIC; whenever a red dot and a blue dot superimpose they were turned into black. (d) Scatter plot of $\log_{10}(E)$ versus $\log_{10}(\Delta Z)$. (e) Normalized histograms of $\log_{10}(E)$; same representation as for $\log_{10}(\Delta Z)$ in (a); the parameters of the fit with the sum of 2 Gaussian distributions are for CML cells: $\alpha = 0.34$ and $\mu_1 = 2.15, \sigma_1 = 0.40, \mu_2 = 2.89, \sigma_2 = 0.51$, and for healthy cells: $\alpha = 0.26$, and $\mu_1 = 2.14, \sigma_1 = 0.34, \mu_2 = 2.87, \sigma_2 = 0.41$ (table 1). (f) Same as (e) but in a logarithmic representation.

small force drop and low released energy failures, and to subpopulation 2 of large indentation depth, long duration, large force drop and high released energy failures. We will classify the former as *ductile* and the latter as *brittle* rupture events.

2.3. Log-normal statistics of released energy during rupture events

The pertinence of the fitting of the p.d.f. of $\log_{10}(E)$ (figure 2(e)) by the sum of 2 Gaussians is compelling when using a logarithmic representation (figure 2(f)). For the CML cells, when fixing the relative percentages of ductile ($1 - \alpha = 0.66$) and brittle ($\alpha = 0.34$) rupture events as previously estimated, we obtained the parameter values reported in table 1 with the following arithmetic and geometric means $\overline{E_1} = 216$ k_BT (resp. $\overline{E_2} = 1547$ k_BT),

Table 1. Distributions of energy released during ductile and brittle rupture events in normal and CML cells: simulations versus experiments. Characteristics ($\overline{N}, \sigma_N, \mu = \overline{\log_{10}(E)}, \sigma = \sigma_{\log_{10}E}, \overline{E}, \tilde{E}$) of the numerical cascades simulated with equation (2) for parameters values a_0, $\hat{a}$, $\Delta E_0 = 12\ k_BT$, $\Delta E^* = 4\ k_BT$ versus experimental data (figures 2(e) and 2(f)).

	Normal Cells	CML Cells
Ductile		
Model parameters	$a_0 = 1.3, \hat{a} = 15, \Delta a = 0.39$	$a_0 = 1.3, \hat{a} = 15, \Delta a = 0.48$
Simulations	$\overline{N} = 9, \sigma_N = 3$	$\overline{N} = 8, \sigma_N = 4$
	$\mu_1 = 2.17, \sigma_1 = 0.31$	$\mu_1 = 2.13, \sigma_1 = 0.38$
	$\overline{E_1} = 191\ k_BT, \tilde{E}_1 = 148\ k_BT$	$\overline{E_1} = 198\ k_BT, \tilde{E}_1 = 135\ k_BT$
Experiments	$\mu_1 = 2.14, \sigma_1 = 0.34$	$\mu_1 = 2.15, \sigma_1 = 0.40$
	$\overline{E_1} = 188\ k_BT, \tilde{E}_1 = 138\ k_BT$	$\overline{E_1} = 216\ k_BT, \tilde{E}_1 = 141\ k_BT$
Brittle		
Model parameters	$a_0 = 1.3, \hat{a} = 46, \Delta a = 0.35$	$a_0 = 1.3, \hat{a} = 53, \Delta a = 0.38$
Simulations	$\overline{N} = 21, \sigma_N = 7$	$\overline{N} = 22, \sigma_N = 8$
	$\mu_2 = 2.84, \sigma_2 = 0.42$	$\mu_2 = 2.92, \sigma_2 = 0.47$
	$\overline{E_2} = 1104\ k_BT, \tilde{E}_2 = 692\ k_BT$	$\overline{E_2} = 1494\ k_BT, \tilde{E}_2 = 832\ k_BT$
Experiments	$\mu_2 = 2.87, \sigma_2 = 0.41$	$\mu_2 = 2.89, \sigma_2 = 0.51$
	$\overline{E_2} = 1158\ k_BT, \tilde{E}_2 = 741\ k_BT$	$\overline{E_2} = 1547\ k_BT, \tilde{E}_2 = 776\ k_BT$

and $\tilde{E}_1 = 141\ k_BT$ (resp. $\tilde{E}_2 = 776\ k_BT$). For normal cells, when fixing $\alpha = 0.26$ ($1 - \alpha = 0.74$), we ended with consistent parameter values (table 1) with $\overline{E_1} = 188\ k_BT$ (resp. $\overline{E_2} = 1158\ k_BT$), and $\tilde{E}_1 = 138\ k_BT$ (resp. $\tilde{E}_2 = 741\ k_BT$). Note that the standard deviations of the Gaussian distributions for $\log_{10}(E)$ are slightly larger for CML than for normal cells and this for both ductile and brittle events.

When comparing the mean released energies during ductile (~200 k_BT) and brittle (~1300 k_BT) rupture events to the dissociation energies of α-actinin/actin binding (~4.3 k_BT) and of filamin/actin binding (~3.6 k_BT) [46], we obtain rough estimates for the number of ABP unbindings during ductile (~50) and brittle (~325) rupture events. Thus, more than 6 times energy is released during brittle failures that last (~50 ms) not more than twice the duration (~30 ms) of ductile failures, meaning that the mean rate of released energy is significantly higher during brittle failures. Interestingly, the computation of the global G_g and initial G_i shear moduli (see figure S1 (see footnote 11)) confirms that CML cells are stiffer ($\overline{G_g} = 1.13 \pm 0.31$ kPa, $\overline{G_i} = 0.77 \pm 0.26$ kPa) than normal ones ($\overline{G_g} = 0.42 \pm 0.05$ kPa, $\overline{G_i} = 0.28 \pm 0.05$ kPa) [36]. In particular, about 37% of FICs bear mean shear relaxation moduli (G_g) larger than 1 kPa in CML cells with very low (7%) counter part in normal cells (see figure S5 (see footnote 11)). Altogether, these observations show that CML cells display a significant proportion of highly tensed perinuclear zones propitious to localized brittle failures by disruption of cross-linked CSK domains impeding complete shape recovery after deformation. This interpretation is strengthened by the experimental observation of an important structural alteration of the actin CSK of immature TF1 cells consecutive to BCR-ABL oncogene transduction. In particular, confocal fluorescence microscopy revealed that in this model of human CML [40–45], juxtanuclear actin aggregates were found in almost 30% of the BCR-ABL-transduced TF1 cells at the expense of the cortical F-actin [43, 45] (figure 3(b)). Very likely, these solid structures were induced by the oncogene since they were rarely observed in the parental TF1 cell line (figure 3(a)).

3. Computational model

To account for the observed log-normal released energy distributions (figures 2(e) and (f)), we propose a multiplicative cascade description of CSK failure events that is inspired from pioneering works on population growth dynamics [47–49].

3.1. Fat tail probability distribution functions: log-normal versus power-law distributions

P.d.f.s with heavy tails have been widely observed in various domains of fundamental and applied sciences [50]. The most popular fat-tail distributions are power-law and log-normal distributions that often have been considered as competing models of experimental data [48, 49]. Power-law distributions are commonly thought to be a statistical characteristics of systems that display space and/or time scale invariance properties [50] with as notable examples scale-free networks [51] and self-organized critical systems [52–54]. Log-normal distributions are paradigmatic fat-tail distributions generated by self-similar fragmentation and more generally multiplicative processes [55, 56] with as historical example the energy cascade model of fully developed turbulence [57]. But, as originally proposed by Kesten [47], power-law and log-normal distributions are indeed intrinsically connected when combining multiplicative and additive random processes:

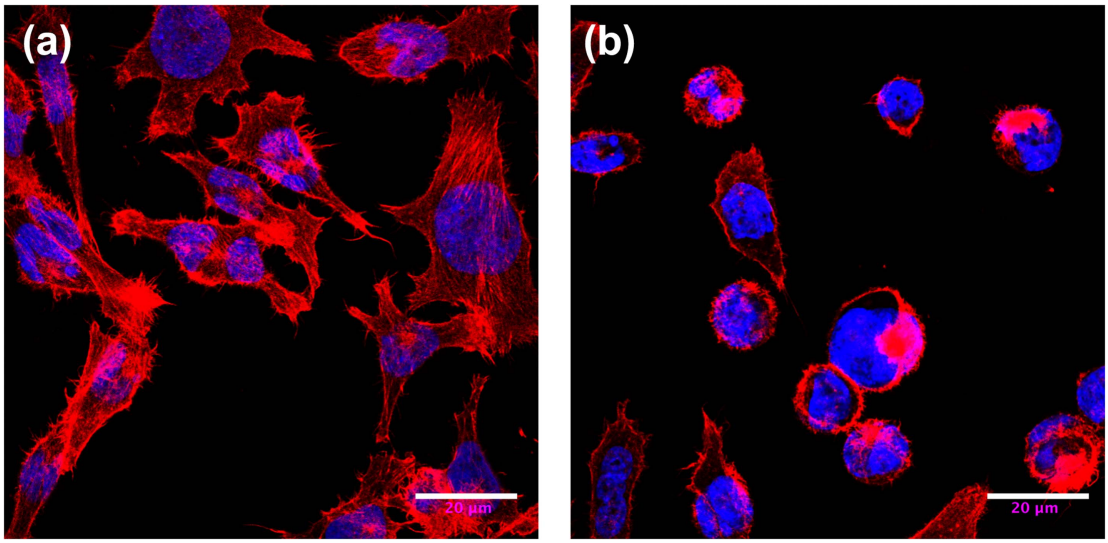

Figure 3. Cytoskeleton structure of TF1 cells revealed by confocal microscopy. (a) Parental TF1 cells. (b) TF1 hematopoietic cells after transfection by the CML BCR-ABL oncogene. F-actin was labeled with phalloidin-rhodamin (red), and the nuclei were labeled with DAPI (blue). Immunofluorescence images were taken using a confocal microscope on fixed TF1 and TF1-BCR-ABL adherent cells on fibronectin (see appendix A). Scale bar: 20 μm.

$$S_t = a_t S_{t-1} + b_t, \tag{1}$$

where S_t is the size of a population at time t, a_t the random positive growth factor, and b_t a small positive random increment. In the absence of the additive b_t term, one recovers the multiplicative Gibrat's law [58] of proportional growth which is nothing but a random walk in log-size leading to a log-normal distribution of S_t. But this distribution is not stable since when the time increases the process S_t either asymptotically shrinks stochastically to zero ($\overline{\ln(a_t)} < 0$) or diverges to infinity ($\overline{\ln(a_t} > 0$). Kesten [47] showed that provided ($\overline{\ln(a_t)} < 0$), adding the random variable b_t prevents the divergence of the log-normal distribution of S_t which progressively switches and converges to a stationary power-law distribution with exponent α given by the strictly positive solution of the equation $\overline{a_t^{\alpha}} = 1$.

3.2. A log-normal released energy cascade model

Our model of CSK cascading rupture events is deliberately reductionist with a minimal number of parameters. At the cascade step $n + 1$, the energy released ΔE_{n+1} satisfies a Gibrat's multiplicative law [58], meaning that it can be expressed as a percentage of the energy ΔE_n released at the previous cascade step:

$$\Delta E_{n+1} = a_n \Delta E_n, \quad \text{with } a_n \sim \mathcal{N}(a_0 \mathrm{e}^{-n/\hat{a}}, \Delta a^2), \tag{2}$$

where a_n is a Gaussian random variable with initial value $a_0 > 1$, whose mean $\overline{a_n}$ decreases exponentially (CSK structural relaxation) with a characteristic depth $\hat{a}$ and a fixed standard deviation $\sigma_{a_n} = \Delta a$. Note that the relationship between the cascade index n and time is not defined in our model since there is no reason *a priori* to assume that the CSK rupture cascade steps occur at regular time intervals. Starting from some initiation threshold ΔE_0, ΔE_n will asymptotically tend to zero because of the exponentially decreasing multiplicative constant a_n which will become smaller than 1 after some finite number of steps. The cascade will end when $\Delta E_{N+1} < \Delta E^*$, where $\Delta E^* \geqslant 0$ is a cascade arrest energy cut-off. During the N steps of the CSK rupture cascade, the total released energy is:

$$E = \sum_{n=1}^{N} \Delta E_n. \tag{3}$$

Our random cascade model mainly depends on three parameters: a_0, $\hat{a}$ and Δa. N is a random variable that depends on the realization of the cascade. Its p.d.f. $P(N)$ is well approximated by a Gaussian distribution (figure 4). To account for the experimental data, all our simulations of the released energy cascade model defined by equation (2) were performed for rather small values of $\Delta a \ll 1$. In this limit, E (equation (3)) can be approximated by:

$$E \simeq E_0 \sum_{n=1}^{N} a_0^n \, \Pi_{i=1}^{n} \mathrm{e}^{-i/\hat{a}} = E_0 \sum_{n=1}^{N} a_0^n \, \mathrm{e}^{-\sum_{i=1}^{n} i/\hat{a}}. \tag{4}$$

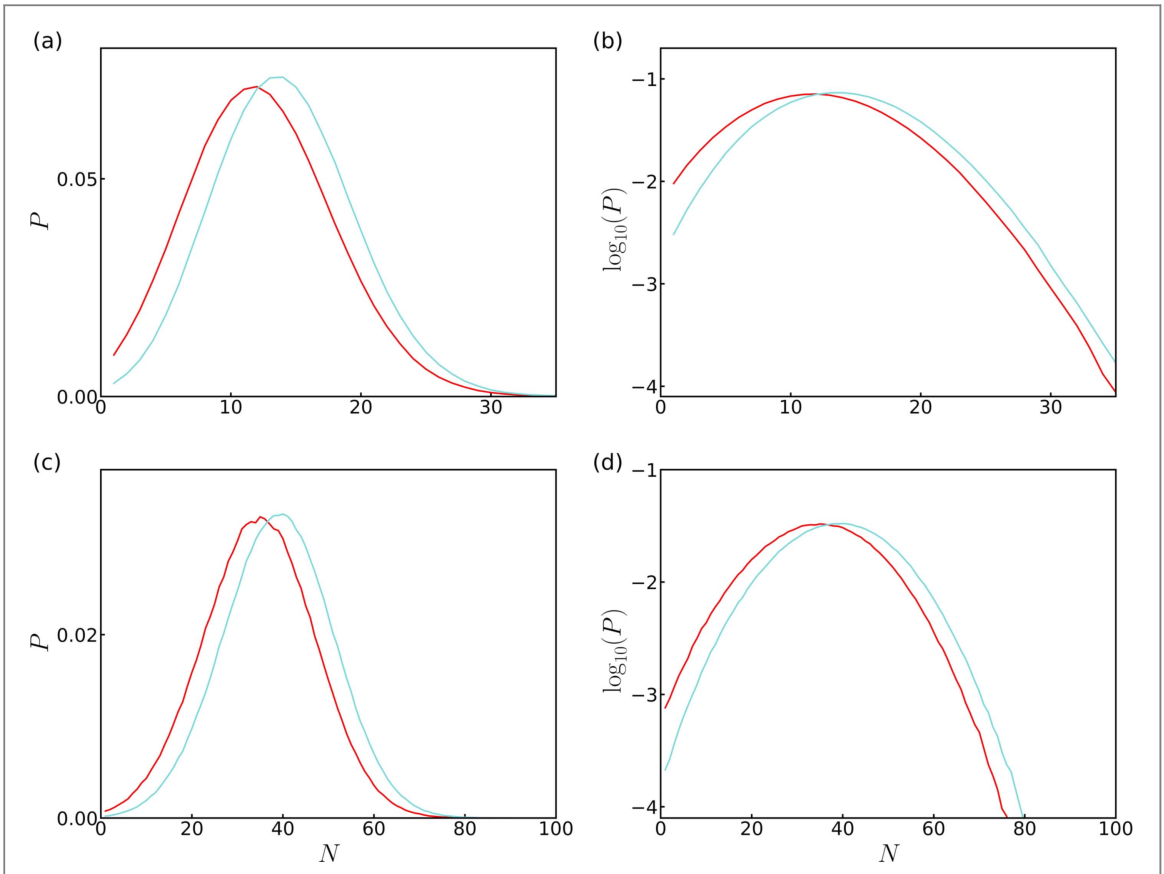

Figure 4. Distributions of the number of steps N of the log-normal rupture cascade model. P.d.f. of N computed from 1.2×10^6 realizations of the multiplicative process defined by equation (2), for parameters values given in table S1 (see footnote 11). (a) Ductile rupture events in normal (blue) and CML (red) cells. (b) Semi-log representation. (c) Brittle rupture events in normal (blue) and CML (red) cells. (d) Semi-log representation.

From the well known identity $\sum_{i=1}^{n} i = n(n+1)/2$, we get

$$E \simeq E_0 \sum_{n=1}^{N} a_0^n \, \mathrm{e}^{-\frac{n(n+1)}{2\hat{a}}}. \tag{5}$$

Thus a good approximation of the mean of E can be obtained by replacing N by the nearest integer $[\overline{N}]$ of its mean $\overline{N}$ in equation (5):

$$\overline{E} \simeq E_0 \sum_{n=1}^{[\overline{N}]} a_0^n \, \mathrm{e}^{-\frac{n(n+1)}{2\hat{a}}}. \tag{6}$$

We recall that the p.d.f. of the random variable N was shown to be well approximated by a Gaussian (figure 4). Now from the Taylor expansion of $\ln(E) = \ln(\overline{E}) + (S - \overline{S})/\overline{S}$ at first order, we can show by taking the ensemble average on both sides of this equation that $\ln(\overline{E})$ is well approximated by

$$\overline{\ln(E)} \approx \ln(\overline{E}). \tag{7}$$

We have confirmed numerically the pertinence of this approximation in all our simulations with a rather good accuracy (<5% error). Now, if we assume that the energy cascade ends when the difference between $\overline{\Delta E_n}$ and the threshold ΔE^* is of the order of Δa, i.e. $a\mathrm{e}^{-\overline{N}/\hat{a}} \simeq K\Delta a$, then

$$\overline{N} \simeq \hat{a} \ln\left(\frac{a_0}{K\Delta a}\right), \tag{8}$$

where K is a constant that has been numerically estimated of order 1 (e.g. $K = 1.52 \pm 0.05$ for $a_0 = 1.3$, $\hat{a} = 45$ and $\Delta a = 0.36$, see figure 5). Equation (8) shows that the mean size $\overline{N}$ of the energy cascade increases as expected when increasing a_0 and $\hat{a}$, but decreases when increasing Δa, since the probability to have a $\Delta E_n < \Delta E^*$ after a limited number n of cascade steps increases (see figure S6 (see footnote 11)).

3.3. Theoretical considerations based on Beaulieu's mathematical results

In our simulations, we fixed $a_0 = 1.3$ and started iterating equation (2) with the initial threshold $\Delta E_0 = 12\ \mathrm{k_B T}$. Note that ΔE_0 is a multiplicative factor that only shifts the p.d.f. of $\log_{10}(E)$ without affecting its shape. When

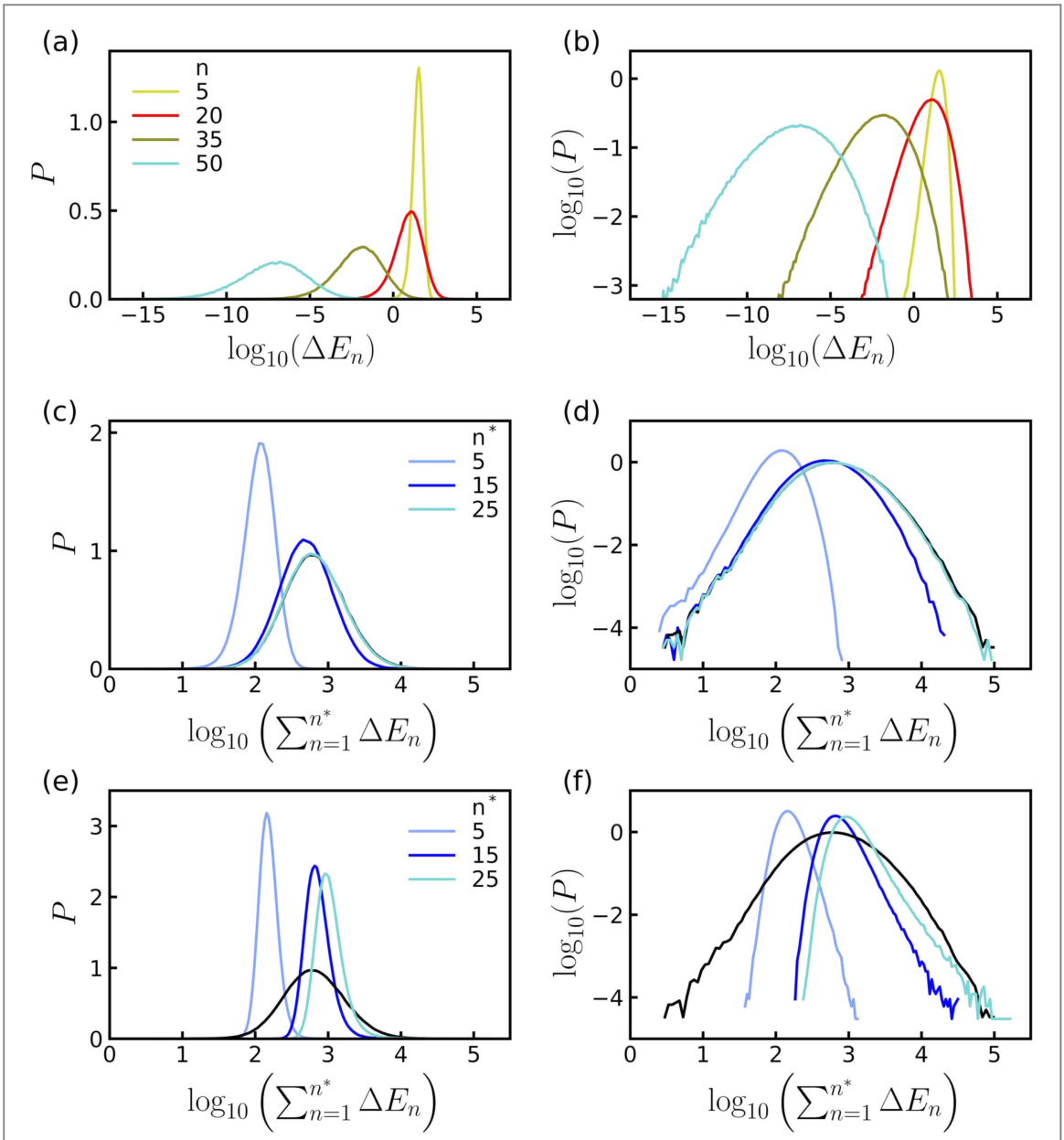

Figure 5. Released energy (k_BT) distributions simulated with the log-normal rupture cascade model. (a) P.d.f. of $\log_{10}(\Delta E_n)$ computed from 1.2×10^6 realizations of the multiplicative process defined by equation (2), for parameters values: $a_0 = 1.3$, $\hat{a} = 45$, $\Delta a = 0.36$, $\Delta E_0 = 12\ k_BT$ and $\Delta E^* = 0$. The colors correspond to $n = 5$ (yellow), 20 (red), 35 (dark green), 50 (cyan); $P(E)$ (black) is shown for comparison. (b) Same as (a) but in a logarithmic representation. (c) P.d.f. of $\log_{10} E_{n^*}$, where $E_{n^*} = \sum_{n=1}^{n^*} \Delta E_n$ for $n^* = 5$ (light blue), 15 (dark blue), 25 (cyan) and N (black). (d) Same as (c) but in a logarithmic representation. (e) Same as (c) but for surrogate uncorrelated released energy cascades (see text). (f) Same as (e) but in a logarithmic representation. In (e) and (f), $P(E_N)$ (black) has the same meaning as in (c) and (d) respectively.

using the cut-off $\Delta E^* = 0$ ($\Delta E_n > 0$, $\forall n$), after some transient ($n \gtrsim 5$), the p.d.f. of ΔE_n obtained from 1.2×10^6 realizations with parameter values $\hat{a} = 45$ and $\Delta a = 0.36$ is well approximated by a log-normal Gibrat's law [58], as expected from multiplicative process (figures 5(a) and (b)). What is more surprising is the fact that the sum E of these log-normal variables turns out also to be well approximated by a log-normal distribution and not by a normal distribution as expected from the central limit theorem. Indeed, this theorem does not apply since the random variables ΔE_n are not only not identically distributed but correlated. Beaulieu [59] has recently proved an extended log-normal limit theorem that states that the limit distribution of the sum of nonidentically distributed correlated log-normal random variables is a log-normal distribution. When investigating how the energy $E_{n^*} = \sum_{n=1}^{n^*} \Delta E_n$, released during the first n^* steps of the cascade converges to the total released energy E_N, we confirmed a rather fast convergence to an asymptotic log-normal distribution (figures 5(c) and (d)). When numerically simulating surrogated uncorrelated released energy cascades where at each step, ΔE_n is randomly generated with the p.d.f. $P(\Delta E_n)$ (figure 5(a)) but independently of the previous cascade steps, then the sum E_{n^*} no longer converges to a log-normal distribution but to a normal distribution as

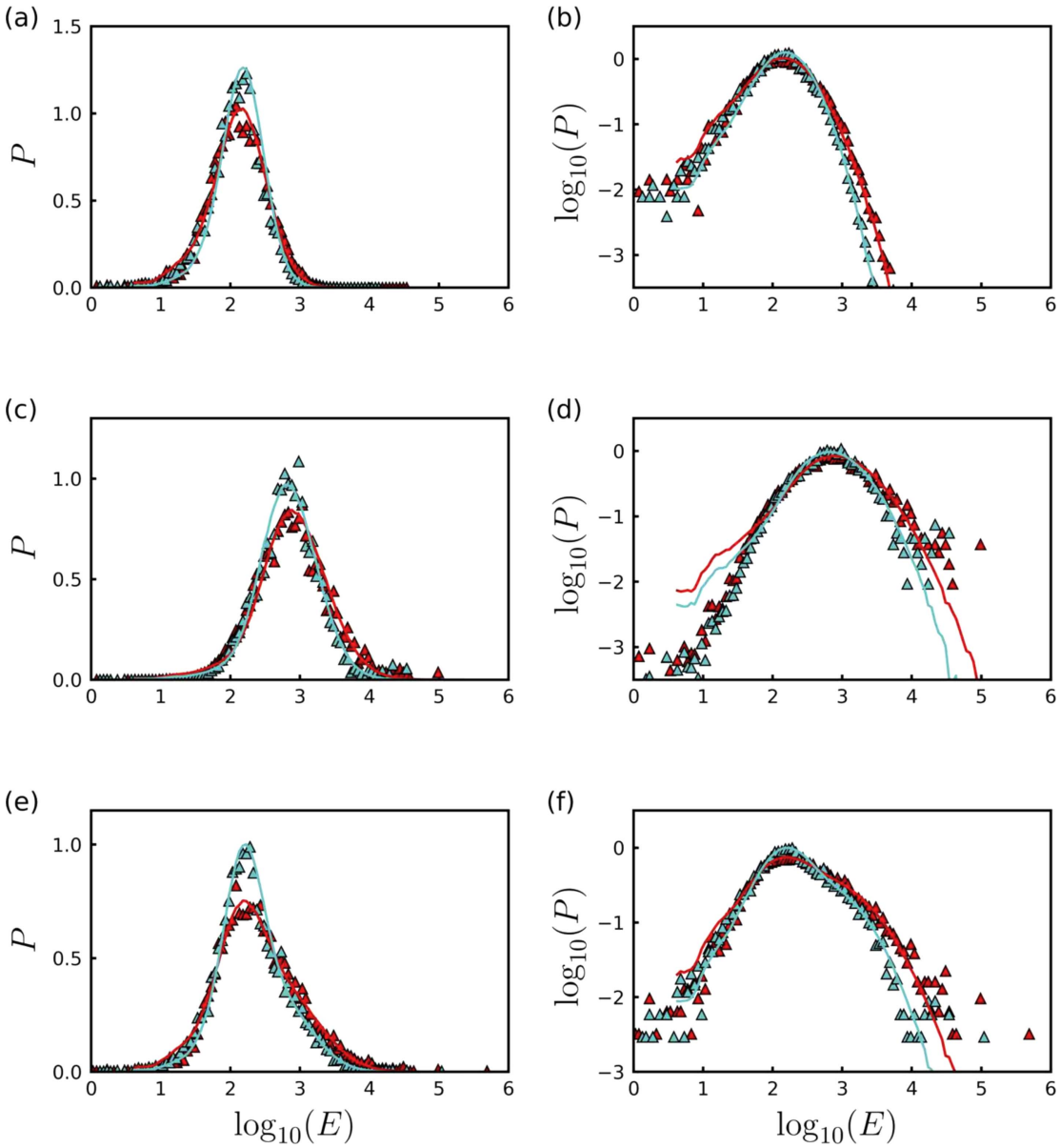

Figure 6. Computed model simulations of the p.d.fs $P(E)$ of energy (k_BT) released during rupture events in normal (blue) and CML (red) cells. Ductile rupture events: (a) semi-log representation; (b) log–log representation. Brittle rupture events: (c) semi-log representation; (d) log–log representation. All rupture events: (e) semi-log representation; (f) log–log representation. The triangles (△) represent the experimental data (figures 2(e) and (f)); ductile and brittle rupture event log-normal p.d.fs were disentangled using a classical two component Gaussian mixture model (see appendix B). The curves represent the prediction of the released energy cascade model defined by equation (2); the corresponding sets of model parameters are given in table 1.

expected for uncorrelated random variables (figures 5(e) and (f)). This theoretical argument suggests that the log-normal distribution observed experimentally (figures 2(e) and (f)) are evidence that the different cascade steps of ABP unbinding are correlated. This theoretical understanding applies to all the numerical simulations reported in this study, for ductile and brittle rupture events, in normal as well as in CML cells (table 1, figures 6 and 7).

3.4. Mechanistic interpretation of ductile and brittle rupture events

We performed numerical simulations of the released energy cascade model to reproduce quantitatively the p.d.fs of E obtained for both normal and CML cells (figures 2(e) and (f)) (see appendix C). To this end, the p.d.f.s corresponding to ductile and brittle rupture events were disentangled with a two component Gaussian mixture model (see appendix B). When fixing $\Delta E_0 = 12\ k_BT$ and $\Delta E^* = 4\ k_BT$ (characteristic unbinding energy of ABPs [46]), sets of parameters (a_0, $\hat{a}$, Δa) values (table 1) were found providing quite satisfactory fits of the experimental released energy distributions (figure 6). For ductile rupture events, the mean number of cascade steps is rather limited for normal ($\overline{N} = 9$) as well as CML ($\overline{N} = 8$) cells and correspond to low mean released

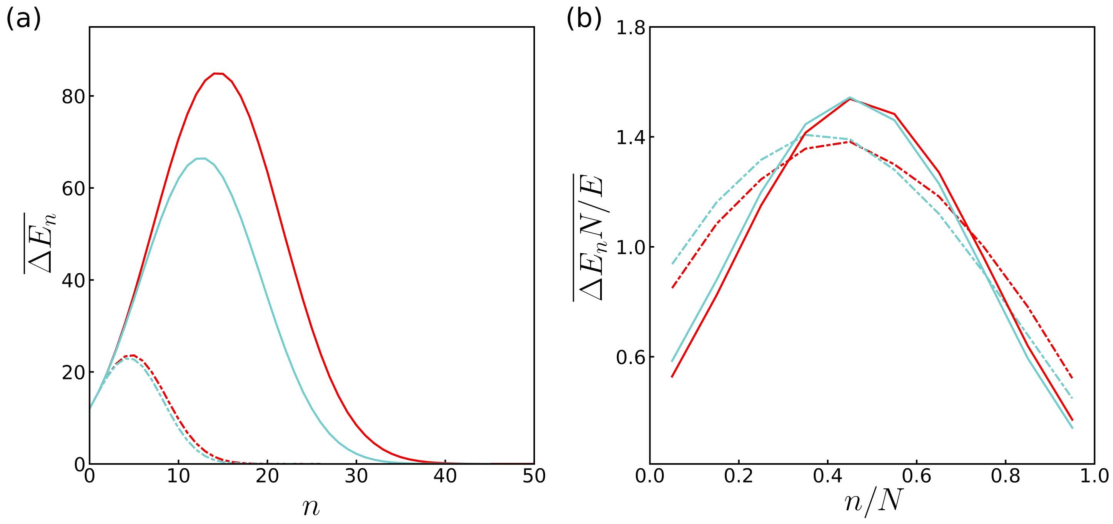

Figure 7. Model predictions for the energy released rate per cascade step (k_BT/step). (a) $\overline{\Delta E_n}$ versus n. (b) $\overline{\Delta E_n/(E/N)}$ versus n/N. The continuous (resp. dotted–dashed) lines correspond to brittle (resp. ductile) rupture events. The colors correspond to normal (blue) and CML (red) cells. The corresponding sets of model parameters are given in table 1.

energy values $\overline{E}$ and likely to a few tens of ABP unbindings ($\overline{N}_{\rm unb} \sim \overline{E}/(4\,k_BT)$) for normal ($\overline{E} = 191\,k_BT$, $\overline{N}_{\rm unb} \sim 48$) and CML ($\overline{E} = 198\,k_BT$, $\overline{N}_{\rm unb} \sim 50$) cells. For brittle failures, our model predicts more expanded cascades with significantly larger values of $\overline{N}$, $\overline{E}$ and $\overline{N}_{\rm unb}$ for both normal ($\overline{N} = 21$, $\overline{E} = 1104\,k_BT$, $\overline{N}_{\rm unb} = 276$) and CML ($\overline{N} = 22$, $\overline{E} = 1494\,k_BT$, $\overline{N}_{\rm unb} \sim 373$) cells (table 1). Besides confirming that brittle rupture events involve more ABP unbindings than ductile ones, our rupture cascade model also predicts that the rate of energy released during the first cascade steps $\overline{\Delta E_n}$ and the maximum reached before the exponential decrease to zero for large n are much higher for brittle than for ductile rupture events (figure 7(a)). Interestingly, when adimensionalizing ΔE_n by a mean released energy E/N per step and n by the total number of cascade steps (figure 7(b)), the numerical data obtained for ductile events in normal and CML cells superimpose and display a slow increase from ∼0.9 to ∼1.3 during the first part of the cascade before decaying toward the energy cut off. For brittle events, the numerical data for normal and CML cells again superimpose (figure 7(b)), but now exhibit an initial three-fold increase from ∼0.5 to ∼1.5. This initial acceleration of ABP unbindings from ∼2–3 to reach values as high as ∼15–20 unbindings per cascade step in brittle events confirms the existence of some correlation between the ABP unbindings of successive cascade steps that likely results in a collective local disorganization and possible disintegration of the CSK. In comparison, the smoother released energy cascade with only a few ABP unbindings (up to 5) at each cascade step strengthens our interpretation of ductile rupture events as more dynamical and reversible stress-induced cross-linker unbindings that would confer to the cell ductile plasticity to large deformations. We have simplified the discussion here by considering only one energy $\simeq 4\,k_BT$ for the actin cross-linker unbinding events, and grouping the brittle and ductile failures into two groups involving a different number of cross-linker unbinding events. Actually we could have also considered that the actin CSK network includes two populations of cross-linking proteins, namely weak cross-linking proteins that give a ductile failure and tight cross-linking proteins leading to brittle failures. The important physical quantity that is quantitatively predicted by the model is the total energy E released during a cascade of rupture events.

We refer the reader to the supplemental material (see footnote 11) where numerical simulations performed with different threshold ΔE_0 (12 and 16 k_BT) and arrest cut-off ΔE^* (0 and 4 k_BT) (see tables S1–S3, and figures S9–S15 (see footnote 11)) confirm the robustness of our rupture cascade model predictions.

4. Discussion

By developing a minimal rupture cascade model, we have identified two distinct populations of singular events in FICs that both correspond to mechanical failures of the CSK with correlated log-normal statistics of released energy. A first type of singular events is associated with rather moderate released energy ($\overline{E} \sim 200\,k_BT$) and likely corresponds to dynamical stress-induced cross-linker unbindings that confer to the cell a ductility preserving the perinuclear CSK architecture. In contrast, the second type of singular events is associated with more dramatic failures that release significantly higher energy ($\overline{E} \sim 1300\,k_BT$) as the signature of irreversible brittle disruption of the CSK integrity in highly tensed perinuclear zones. Besides providing quantitative robust modeling of the observed log-normal statistics, this model predicts that (i) the number of cascade steps, and in

turn the number of cross-linker unbindings, is significantly higher in brittle than in ductile failures, (ii) the released energy increases during the first cascade steps until a maximum value that is significantly higher in brittle than in ductile failures, and (iii) the rate of released energy during these first cascade steps is also significantly higher in brittle than in ductile rupture events. This model further confirms that brittle failures are more frequently observed in CP-CML than in healthy cells as the signature of their higher mechanical fragility under large and fast strain. We anticipate that the mechanistic description provided by our minimal rupture cascade model will apply quite generally to other cell types in physiological and pathological situations [60] and to other nonactive soft matter or solid systems such as biopolymer gels and glassy materials [61]. This minimal model is a very promising first attempt that will be used as a guide for future 2D and 3D simulations, aiming at elucidating the impact of CSK network architecture on the rupture mechanics of living cells.

Acknowledgments

We are indebted to L Berguiga, E Gerasimova-Chechkina, C Martinez-Torres, L Streppa, R Vincent and T Voeltzel for fruitful discussions. We are very grateful to T Muller and to the R&D department of the JPK Company for their partnership. This study was supported by the Joliot Curie and Physics Laboratories (ENS Lyon/CNRS), the Agence Nationale de la Recherche ANR-10-BLAN-1516, INSERM (Plan Cancer 2012 01-84862), Novartis, Ligue Nationale contre le Cancer (Saone et Loire) and Cent pour Cent la Vie. FJPR acknowledges financial support from the Carnegie Trust.

Appendix A. Experimental protocols

A.1. Cell culture and adhesion assay

After informed consent in accordance with the Declaration of Helsinki and local ethics committee bylaws (from the Délégation à la recherche clinique des Hospices Civils de Lyon, Lyon, France), bone marrow samples were obtained from CP-CML patients at diagnosis and from healthy allogeneic donors. Mononuclear cells were separated using a Ficoll gradient (Bio-Whittaker) and were then subjected to $CD34^+$ immunomagnetic separation (Stemcell Technologies). The purity of the $CD34^+$ enriched fraction was checked by flow cytometry and was over 95% on average. Selected bulk $CD34^+$ cells were seeded at 6×10^5 cells ml^{-1} and cultured in serum-free Iscove's Modified Dulbecco's Medium (Invitrogen) in the presence of 15% BSA, insulin and transferrin (Stemcell Technologies) supplemented with 10 ng ml^{-1} interleukin-6 (IL-6), 50 ng ml^{-1} stem cell factor, 10 ng ml^{-1} IL-11 and 10 ng ml^{-1} IL-3 (Peprotech).

To question the possible modifications of mechanical properties of immature hematopoietic cells upon oncogene expression, we have used the TF1 cell line transduced with the BCR-ABL oncogene as a unique model of CML cells that reproduces the early steps of stem cell transformation [40–44, 62–67]. In CML particularly, BCR-ABL is known for its ability to decrease progenitor cell adhesion to stroma [42, 68, 69]. By performing adhesion assays, we observed that BCR-ABL transduction has no effect on the percentage of adhesion of TF1 cells on fibronectin-coated surfaces (data not shown) [70]. This is according to the fact that TF1 cells are representative of very immature cells rather than progenitors of more differentiated cells. The immature $CD34^+$ TF1 cell line (ATCC CRL-2003) was maintained at 1×10^5 cells ml^{-1} in RPMI-1640 medium, 10% fetal calf serum and granulocyte macrophage colony-stimulating factor (10 ng ml^{-1}) (Sandoz Pharmaceuticals). Engineered TF1-GFP and TF1-BCR-ABL-GFP cell lines were obtained by transduction with a murine stem cell virus-based retroviral vector encoding either the enhanced green fluorescent protein cDNA alone (EGFP) as a control or the BCR/ABL-cDNA upstream from an IRES-eGFP sequence [42, 64]. EGFP+ TF1 cells were sorted using a Becton Dickinson FACSAria.

Adhesion was performed as described in [68–70]. Fibronectin (Sigma) was coated for 2 h at 37 °C on 96-well Cellstar dishes (Greiner) using a 50 μg ml^{-1} ligand solution in sodium bicarbonate buffer (0.1 mM). Plates were blocked with 0.3% BSA in PBS for 1 h at 37 °C. Cells (5.10^4/well) were labeled for 20 min at 37 °C with 5 μM calcein-AM (Molecular Probes) in RMPI medium containing 0.1% BSA (without phenol red). Cells were then allowed to adhere to the coated plates in triplicate wells for 1 h at 37 °C in the adhesion buffer (PBS with 0.03% BSA), before removal of the non-adherent fraction. Finally, the glass coverslip was mounted on the AFM stage and the cells were kept in their culture medium at room temperature.

A.2. Immunofluorescence staining

Cells were seeded at 5×10^5 cells ml^{-1} and incubated for 24 h before the experiment. On the one hand, non-adherent cells were centrifuged onto glass slides with a cytospin 4 (Thermo Scientific). On the other hand, non-adherent cells were allowed to adhere on glass cover slips coated with fibronectin (Sigma) in culture treated plates (BD Biosciences/Falcon) for 1 h at 37 °C, before removal of the non-adherent fraction. Cells were then

fixed with 4% paraformaldehyde for 15 min, permeabilized with 0.1% Triton X-100 (Sigma-Aldrich) for 10 min, and blocked with 0.2% gelatin (Sigma-Aldrich) for 30 min at room temperature. The filamentous actin (F-actin) was labeled with 1000-fold diluted phalloidin-rhodamin (Sigma-Aldrich) for 30 min at room temperature. Cells were washed twice and were then incubated for 1 h at room temperature with a 400-fold diluted rabbit polyclonal anti-GFP antibody-Alexa Fluor 488 conjugate (Life Technologies). Finally, cells were washed twice and subsequently the nuclei were labeled with 2000-fold diluted DAPI (Sigma-Aldrich) in mounting medium (Sigma-Aldrich). Controls for nonspecificity and autofluorescence were performed by incubating cells without phallodin-rhodamin or by incubating TF1 cells with the rabbit polyclonal anti-GFP Alexa Fluor 488 conjugate. Fluorescence images were taken using a spectral confocal microscope TCS SP5 AOBS (Leica) (For more details see [45, 70]).

A.3. CSK structure alterations in transduced adherent cells revealed by confocal fluorescence microscopy

To investigate the structural transformation of the actin CSK consecutive to BCR-ABL transduction, we performed two different types of microscopy studies: (i) confocal microscopy [45, 70] on fixed TF1 and TF1-BCR-ABL cells where both F-actin and the nucleus were stained (figure 3), and (ii) quantitative phase microscopy [71–73] from which an important disorganization of the internal cell compartments was put into light by enhanced optical phase gradients. In BCR-ABL-transduced TF1 cells, juxtanuclear actin aggregates were found in almost 30% of the cells in addition to the cortical F-actin staining [45] (figure 3(b)). Very likely these structures were induced by the oncogene since they were rarely observed in the parental TF1 cell line (figure 3(a)). Consistently BCR-ABL-transduced cells showed fewer actin stress fibers as compared to TF1 cells in adhesion. The mechanical confinement of the TF1-BCR-ABL cells onto adherent fibronectin surfaces enlightens the interplay between the oncogene BCR-ABL and actin microfilaments, making their morphological changes quite visible by fluorescence microscopy (figure 3). These observations indicate that transducing TF1 cells with BCR-ABL likely disrupts their actin CSK cohesion and inhibit their crawling motility [45].

A.4. Mechanical indentation experiments and FICs recording

FICs were recorded from AFM cantilever deflection signals, when indenting the cell (approach curves) at fixed scan velocity $V_0 = 1\ \mu\text{m s}^{-1}$ with a CellHesion system equipped with a 15−200 μm motorized stage, from JPK Instruments AG (www.jpk.com) mounted on an inverted microscope. We used pyramidal shape tip cantilevers (SNL-10, Bruker) with a nominal spring constant of 0.06 nN nm^{-1}. Prior to each experiment, the deflection sensitivity of the cantilever was estimated on fused silica and the cantilever spring constant k was calibrated by the thermal noise method in between 0.05 and 0.15 N m^{-1} by directly recording their free fluctuations in buffer solution, computing their power spectrum distribution and fitting these curves with Lorentzian distributions [74]. Cells were prepared by letting suspended cells adhere on glass cover slips coated with fibronectin (Sigma) in culture treated plates (BD Biosciences/Falcon) for 1 h at 37 °C, and the non-adherent fraction was removed before mounting the coverslip on the AFM stage. During AFM recording, the cells were kept in their culture medium at room temperature (24 °C). To reduce variability, indentation was carried out at the center of each cell within 2 h after removing cells from the incubator, to probe the perinuclear CSK that is known to play a protective and mechanical confining role for the underlying nucleus and its multi-scale functions [75]. In all the experiments, cell sizes were evaluated from transmission microscopy images. To avoid these cells slipping away from the cantilever during the indentation, we immobilized them on a fibronectin-coated coverslip before AFM probing. Interaction of the integrins at the cell membrane with the fibronectin-coated surface not only confines cell movements on the glass surface but also modifies its CSK architecture, inducing a cascade of molecular events leading to cell spreading and higher adherence [76]. Actually, this fibronectin adhesion assay mimics to some extent the fact that, under physiological conditions, hematopoietic cells are not in suspension in their human bone marrow niche but actively adhere to the stroma and to proteins of the extracellular matrix [42, 68].

If we define Z as the distance of the cantilever tip to the sample surface: $Z = Z_{\text{tip}} - Z_{\text{surf}}$, the contact point Z_c corresponds to the tip position touching the sample surface without being deflected. Z_c is taken as origin of the FICs in figures 1(c) and (d). Overall, one approach/retract experiment lasts a few seconds, which is shorter than the characteristic remodeling time by active molecular motors. A key issue in the analysis of FICs is the determination of Z_c for very soft materials, like living cells. To master this practical signal-to-noise issue, we used a wavelet-based decomposition of the FICs and their derivatives [36, 39] that likely achieved some compromise between a too strong smoothing of the force derivative that would wipe out the non-contact to contact transition, and a too mild smoothing of the force that would suffer from a noise estimation of the contact points (see figures S2 and S3 (see footnote 11)). Once the cell is deformed by the cantilever, $Z > Z_c$, $Z - Z_c$ reads as the sum of two terms, respectively the cell indentation h and the ratio of the force F and the cantilever spring constant k [77]:

$$Z - Z_c = h + F/k. \tag{A1}$$

The nominal spring constant k of the cantilever ($k = 0.06$ nN nm^{-1}) was chosen large enough for the cantilever deflection to be small compared to the cell deformation. Nevertheless, we have substracted the correcting term from the FICs for energy integral computation. Note that this correcting term does not affect the computation of the second-order derivative of the force.

Appendix B. Time–frequency analysis of FICs

B.1. Historical introduction to the wavelet transform

The wavelet transform is a mathematical time–frequency (time scale) decomposition of signals introduced in the early 1980s [78]. The wavelet transform has been applied to a great variety of situations in physics, physical chemistry, biology, signal and image processing, material engineering, mechanics, economics, epidemics… [75, 79–84]. Real experimental signals are very often nonstationary (they contain transient components), and when they are complex or singular, they may also involve a rather wide range of frequencies. It also happens that experimental signals display characteristic frequencies that drift in time. Standard Fourier analysis is therefore inadequate in these situations, since it provides only statistical information about the relative contributions of the frequencies involved in the analyzed signal. The possibility to perform simultaneously a temporal and frequency decomposition of a given signal was first proposed by Gabor for the theory of communication [85]. Later on, two distinct approaches (based on different wavelet transforms) were developed in parallel: (i) a continuous wavelet transform (CWT) [78, 82] and (ii) a discrete wavelet transform [80]. For singular (self-similar or multi-fractal) signals or images, the CWT transform rapidly became a predilection mathematical microscope to perform space (or time)-scale analysis and to characterize scale invariance properties. In particular it was used to generalize box-counting techniques [86] and to remedy the limitations of structure function methods [87] in elaborating a statistical physics formalism of multifractals [81, 84, 87–92].

During the past 30 years, the CWT was used for biological applications, on both 1D signals and 2D images [75, 83, 84, 93–107]. As far as 1D signals are concerned, the CWT was applied to AFM force curves collected from single living plant cells [39], living hematopoietic stem cells [36, 45] and to AFM fluctuation signals to characterize the passive microrheology of living myoblasts [108]. The 1D CWT was also generalized to 2D (and to 3D) CWT [79, 83, 84, 96] and it proved again its versatility and power for analyzing AFM topographic images of biosensors [109], fluorescence microscopy images of chromosome territories [98] and diffraction phase microscopy of living cells [71–73].

B.2. Wavelet-based decomposition of FICs

Viscoelastic theories developed during the second half of the twentieth century have led to general hereditary integral representation of stress-strain relationships for the indentation of linear viscoelastic materials by axisymmetric indenters [110]:

$$F(t) = \frac{4}{1-\nu} C_n \int_0^t G(t-\tau) \frac{\mathrm{d}h^{(n+1)/n}(\tau)}{\mathrm{d}\tau} \mathrm{d}\tau, \tag{B1}$$

where $G(t)$ is the stress relaxation modulus, F is the loading force, h describes the displacement of the indenter and n is a positive integer which depends on the shape of the indenter. The stress relaxation modulus $G(t)$ retains the strain-rate memory of the deformation. For a pyramidal indenter tip [38], we have $n = 1$ and $C_1 = \tan\theta/\pi$, where θ is the nominal tip half-angle:

$$F(t) = \frac{4\tan\theta}{\pi(1-\nu)} \int_0^t G(t-\tau) \frac{\mathrm{d}h^2(\tau)}{\mathrm{d}\tau} \mathrm{d}\tau. \tag{B2}$$

Since the cantilever is swept at constant velocity V_0, $\mathrm{d}Z = V_0 \mathrm{d}t$, the stress relaxation modulus G can be rewritten as:

$$G(Z) = \frac{\pi(1-\nu)}{8\tan\theta} \frac{\mathrm{d}^2 F(Z)}{\mathrm{d}Z^2}, \tag{B3}$$

meaning that the change of G with Z is an important quantity that is stored in the whole deformation story. This relation establishes that the stress relaxation modulus can be obtained from the second derivative of the indentation force curve with respect to Z, without assuming *a priori* a particular viscoelastic or plastic cellular model.

Practically, we used a time–frequency adaptative wavelet-based method to compute $G(Z)$ from FICs. Within the norm $\mathcal{L}^1$, the one-dimensional WT of a signal $F(Z)$ reads [78–82]:

$$W_{\psi}[F](b,\,s) = \frac{1}{s}\int_{-\infty}^{\infty} F(Z)\psi^{*}\left(\frac{Z-b}{s}\right)\mathrm{d}Z, \tag{B4}$$

where b is a spatial coordinate (homologous to Z) and $s\,(>0)$ a scale parameter. In the context of this study, we concentrated on the family of analyzing wavelets obtained from the successive derivatives of the Gaussian function [75, 81–84] (see figure S2(a) (see footnote 11)):

$$g^{(0)}(Z) = \mathrm{e}^{-Z^2/2}. \tag{B5}$$

Let us define the first derivative of the Gaussian function (see figure S2(b) (see footnote 11)):

$$g^{(1)}(Z) = -\frac{\mathrm{d}}{\mathrm{d}Z}g^{(0)}(Z) = Z\mathrm{e}^{-Z^2/2}, \tag{B6}$$

and its second derivative, also called the Mexican hat wavelets (see figure S2(c) (see footnote 11)):

$$g^{(2)}(Z) = -\frac{\mathrm{d}^2}{\mathrm{d}Z^2}g^{(0)}(Z) = \mathrm{e}^{-Z^2/2}(1-Z^2). \tag{B7}$$

Via one (resp. two) integration(s) by part, it is straightforward to demonstrate [75, 81–84, 90] that the WT of F with the first (resp. the second) derivative of a Gaussian wavelet at scale s, $W_{g^{(1)}}[F](b,\,s)$ (resp. $W_{g^{(2)}}[F](b,\,s)$) is precisely the first (resp. second) derivative of a smooth version $W_{g^{(0)}}[F](b,\,s)$ of F by a Gaussian function at the same scale s:

$$W_{g^{(1)}}[F](b,\,s) = s\frac{\mathrm{d}}{\mathrm{d}b}W_{g^{(0)}}[F](b,\,s), \tag{B8}$$

and

$$W_{g^{(2)}}[F](b,\,s) = s^2\frac{\mathrm{d}^2}{\mathrm{d}b^2}W_{g^{(0)}}[F](b,\,s). \tag{B9}$$

Let us point out that the validity of the WT definition (equation (B4)) was further extended for distributions including Dirac distributions [81, 82, 90, 111]. The interest of the WT method is two-fold. The first advantage is to use the same smoothing function to filter out the experimental background noise and to compute higher-order derivatives (for instance up to second-order in this study) at a well defined smoothing scale s_g. The second advantage relies on the power of the WT to detect local singularities (including rupture events in the FICs) and to quantify their force via the estimate of local Hölder exponents from the behavior across scales of the WT modulus maxima [75, 81–84, 87–92]. In this study, we used modified versions [45] of the definition (equation (B4)) of the WT to get a direct measure of F in nN ($T_{g^{(0)}}[F](b,\,s)$), $\mathrm{d}F/\mathrm{d}Z$ in nN nm^{-1} ($T_{g^{(1)}}[F](b,\,s)$) and $\mathrm{d}^2F/\mathrm{d}Z^2$ in Pascal ($T_{g^{(2)}}[F](b,\,s)$), once smoothed by a Gaussian window ($g^{(0)}(Z)$) of width s:

$$T_{g^{(0)}}[F](b,\,s) = W_{g^{(0)}}[F](b,\,s), \tag{B10}$$

$$T_{g^{(1)}}[F](b,\,s) = \frac{1}{s}W_{g^{(1)}}[F](b,\,s), \tag{B11}$$

$$T_{g^{(2)}}[F](b,\,s) = \frac{1}{s^2}W_{g^{(2)}}[F](b,\,s). \tag{B12}$$

Figure S3 (see footnote 11) illustrates on a single FIC (approach and retract curves) the computation of the wavelet-based force derivatives. Let us point out that from equations (B1)–(B3), we get the following expression for the stress relaxation modulus [36, 39, 45]:

$$G(Z) = \frac{\pi(1-\nu)}{8\tan\theta}T_{g^{(2)}}[F](Z,\,s). \tag{B13}$$

B.3. Tracking the rupture events in FICs

The protocol that we have elaborated to track singular events in FICs is shown in figures 1(e) and (f). The optimal wavelet scale to compute $G(Z)$ via equation (B13) was fixed to $w = 2\sqrt{2}\,s = 42$ nm. Noticing that the FIC disruption events occurred in between two consecutive minima G_m and maxima G_M of $\mathrm{d}^2F(Z)/\mathrm{d}Z^2$ (figure 1(f)), we took the local minima G_m as searching criteria. We defined a threshold $|G_m|$ for the distribution of G_m values computed on a representative set of FICs, to discriminate the disruption events from the background noise. The prominence of these negative peaks was set to $|G_m| \geqslant 50$ kPa. In the right neighborhood of these peaks, we searched for a local maxima of $\mathrm{d}^2F(Z)/\mathrm{d}Z^2$ with a peak prominence $\geqslant$20 kPa. G_m and G_M are marked by black symbols in figure 1(f). From the two positions of G_m and G_M we could then detect the beginning and the end of the disruption events represented by blue symbols in figure 1(e). The distance between these two positions was denoted as ΔZ. Finally, the force drop ΔF was corrected, taking into account the increasing trend

of the FIC after the rupture event. A linear interpolation of the FIC in a small interval (~30 nm) beyond the local minima of the FIC gave the best interpolation.

B.4. Statistical analysis of rupture events in FICs

The normalized histograms obtained for $\log_{10}(\Delta Z)$, $\log_{10}(\Delta F)$ and $\log_{10}(E)$ for the rupture events detected in the two sets of FICs from healthy and CML cells were fitted (nonlinear least square fit method) by the sum of two Gaussian distributions:

$$P(Y) = \frac{(1 - \alpha)\exp\left[\frac{-(Y - \mu_1)^2}{2\sigma_1^2}\right]}{\sqrt{2\pi}\,\sigma_1} + \frac{\alpha \exp\left[\frac{-(Y - \mu_2)^2}{2\sigma_2^2}\right]}{\sqrt{2\pi}\,\sigma_2}, \tag{B14}$$

where the indices 1 and 2 refer to ductile and brittle rupture events respectively. μ_1 (resp. μ_2) and σ_1 (resp. σ_2) are the mean and root-mean-square of the random variable $Y = \log_{10}(X)$. The arithmetic and the geometry means of X are $\overline{X} = E[X] = 10^{\mu + \ln(10)\sigma^2/2}$ and $\tilde{X} = GM[X] = 10^{\mu}$ respectively. The parameter α in equation (B14) quantifies the statistical contribution (%) of brittle events as compared to the contribution $1 - \alpha$ (%) of ductile rupture events. In figure 6, a two component Gaussian mixture model was used to disentangle the p.d.fs of $\log_{10}(E)$ corresponding to brittle rupture events and ductile rupture events.

Appendix C. Simulations of the released energy cascade model

To mimic the released energy distributions observed experimentally for both ductile and brittle rupture events, in normal and CML cells (figures 2(e) and (f)), we have generated 1.2×10^6 realizations of the multiplicative process defined by equation (2) using $\Delta E_0 = 12\ k_BT$ as initial threshold and $\Delta E^* = 0$ (figures 4, 5, and also figures S6, S7 and S12 and table S1 (see footnote 11)) or $4\ k_BT$ (figure 6, table 1) as the energy cascade arrest cut-off ($\Delta E_{N+1} < \Delta E^*$). For $\Delta E^* = 0$, we have systematically investigated the dependence of the p.d.fs of the number of cascade steps N and of the corresponding released energy E on the three parameters a_0, $\hat{a}$ and Δa. As long as $\overline{N}$ is not too small, $P(N)$ is well approximated by a Gaussian distribution (figure 4) whose mean increases when increasing a_0 or $\hat{a}$, or when decreasing Δa, fixing the two other parameters (see figure S6 (see footnote 11)), in good agreement with the theoretical prediction (equation (8)). Interestingly, the corresponding $P(E)$ turns out to be well approximated by a log-normal distribution (figures 5(a) and (b)). When using the parameter dependence of $\overline{\log_{10} E}$ and $\overline{\sigma}_{\log_{10}(E)}$ versus a_0, $\hat{a}$ and Δa (see figure S7 (see footnote 11)), we realized that we could fit the experimental log-normal distributions by fixing $a_0 = 1.3$ (>1) and adjusting $\hat{a}$ and Δa to match the parameters μ_i and σ_i estimated from log-normal fits of the data for ductile and brittle events in both normal and CML cells (see figure S12 and table S1 (see footnote 11)). When using a finite energy cut-off $\Delta E^* = 4\ k_BT$ consistent with the experimental estimate of ABP unbinding energy [46], we still were able to quantitatively reproduce the log-normal distributions of released energy observed experimentally for parameter values reported in table 1 (figure 6). Note that with this finite ΔE^* cut-off, some departure from Gaussian tail is observed in $P(N)$ for small N (see figure S10 (see footnote 11)), and in turn in $P(\log_{10}(E))$ for small $\log_{10}(E)$ values (figure 6), as the signature of a lack of statistical convergence of the shortest rupture cascades. Interestingly this departure seems also to be present in the experimental $P(\log_{10}(E))$ distributions (figure 6).

References

[1] Hoffman B D and Crocker J C 2009 Cell mechanics: dissecting the physical responses of cells to force *Annu. Rev. Biomed. Eng.* **11** 259–88

[2] Chauviere A, Preziosi L and Verdier C (ed) 2010 *Cell Mechanics: From Single Scale-Based Models to Multiscale Modeling* (Boca Raton, FL: CRC Press)

[3] Brunner C, Niendorf A and Käs J A 2009 Passive and active single-cell biomechanics: a new perspective in cancer diagnosis *Soft Matter* **5** 2171–8

[4] Kai F, Laklai H and Weaver V M 2016 Force matters: biomechanical regulation of cell invasion and migration in disease *Trends Cell Biol.* **26** 486–97

[5] Fabry B, Maksym G, Butler J, Glogauer M, Navajas D and Fredberg J 2001 Scaling the microrheology of living cells *Phys. Rev. Lett.* **87** 148102

[6] Hoffman B D, Massiera G, Van Citters K M and Crocker J C 2006 The consensus mechanics of cultured mammalian cells *Proc. Natl Acad. Sci. USA* **103** 10259–64

[7] Gardel M L, Kasza K E, Brangwynne C P, Liu J and Weitz D A 2008 Mechanical response of cytoskeletal networks *Methods Cell Biol.* **89** 487–519

[8] Lieleg O, Claessens M M A E and Bausch A R 2010 Structure and dynamics of cross-linked actin networks *Soft Matter* **6** 218–25

[9] Kollmannsberger P and Fabry B 2011 Linear and nonlinear rheology of living cells *Annu. Rev. Mater. Res.* **41** 75–97

[10] Broedersz C P and Mackintosh F C 2014 Modeling semiflexible polymer networks *Rev. Mod. Phys.* **86** 995–1036

[11] Rigato A, Miyagi A, Scheuring S and Rico F 2017 High-frequency microrheology reveals cytoskeleton dynamics in living cells *Nat. Phys.* **13** 771–5

[12] Wagner B, Tharmann R, Haase I, Fischer M and Bausch A R 2006 Cytoskeletal polymer networks: the molecular structure of cross-linkers determines macroscopic properties *Proc. Natl Acad. Sci. USA* **103** 13974–8
[13] Broedersz C P, Storm C and MacKintosh F C 2008 Nonlinear elasticity of composite networks of stiff biopolymers with flexible linkers *Phys. Rev. Lett.* **101** 118103
[14] Kollmannsberger P, Mierke C T and Fabry B 2011 Nonlinear viscoelasticity of adherent cells is controlled by cytoskeletal tension *Soft Matter* **7** 3127–32
[15] Fletcher D A and Mullins R D 2010 Cell mechanics and the cytoskeleton *Nature* **463** 485–92
[16] Huber F, Schnauss J, Ronicke S, Rauch P, Muller K, Futterer C and Käs J 2013 Emergent complexity of the cytoskeleton: from single filaments to tissue *Adv. Phys.* **62** 1–112
[17] Blanchoin L, Boujemaa-Paterski R, Sykes C and Plastino J 2014 Actin dynamics, architecture and mechanics in cell motility *Physiol. Rev.* **94** 235–63
[18] Ehrlicher A J, Krishnan R, Guo M, Bidan C M, Weitz D A and Pollak M R 2015 Alpha-actinin binding kinetics modulate cellular dynamics and force generation *Proc. Natl Acad. Sci. USA* **112** 6619–24
[19] Julicher F, Kruse K, Prost J and Joanny J F 2007 Active behavior of the cytoskeleton *Phys. Rep.* **449** 3–28
[20] Dos Remedios C G, Chhabra D, Kekic M, Dedova I V, Tsubakihara M, Berry D A and Nosworthy N J 2003 Actin binding proteins: regulation of cytoskeletal microfilaments *Physiol. Rev.* **83** 433–73
[21] Tseng Y, Kole T P, Lee J S H, Fedorov E, Almo S C, Schafer B W and Wirtz D 2005 How actin crosslinking and bundling proteins cooperate to generate an enhanced cell mechanical response *Biochem. Biophys. Res. Commun.* **334** 183–92
[22] Esue O, Tseng Y and Wirtz D 2009 Alfa-actinin and filamin cooperatively enhance the stiffness of actin filament networks *PLoS One* **4** 1–6
[23] Winkelman D, Suarez C, Hocky G M, Harker A J, Morganthaler A N, Christensen J R, Voth G A, Bartles J R and Kovar D R 2016 Fascin- and alpha-actinin-bundled networks contain intrinsic structural features that drive protein sorting *Curr. Biol.* **26** 2697–706
[24] Wolff L, Fernandez P and Kroy K 2010 Inelastic mechanics of sticky biopolymer networks *New J. Phys.* **12** 053024
[25] Gralka M and Kroy K 2015 Inelastic mechanics: a unifying principle in biomechanics *Biochim. Biophys. Acta* **1853** 3025–37
[26] Fredberg J J, Inouye D, Miller B, Nathan M, Jafari S, Raboudi S H, Butler J P and Shore S A 1997 Airway smooth muscle, tidal stretches, and dynamically determined contractile states *Am. J. Respir. Crit. Care Med.* **156** 1752–9
[27] Bonakdar N, Gerum R, Kuhn M, Spörrer M, Lippert A, Schneider W, Aifantis K E and Fabry B 2016 Mechanical plasticity of cells *Nat. Mater.* **15** 1090–5
[28] Song Y, Chen X, Dabade V, Shield T W and James R D 2013 Enhanced reversibility and unusual microstructure of a phase-transforming material *Nature* **502** 85–8
[29] Antonaglia J, Xie X, Schwartz G, Wraith M, Qiao J, Shang Y, Liaw P K, Uhl J T and Dahmen A 2014 Tuned critical avalanche scaling in bulk metallic glasses *Sci. Rep.* **4** 4382
[30] Perez-Reche F J 2017 Modeling avalanches in martensites *Avalanches in Functional Materials and Geophysics* ed E K H Salije *et al* (Dordrecht: Springer) pp 99–136
[31] Radmacher M 2002 Measuring the elastic properties of living cells by the atomic force microscope *Methods Cell Biol.* **68** 67–90
[32] Mahaffy R E, Park S, Gerde E, Käs J and Shih C K 2004 Quantitative analysis of the viscoelastic properties of thin regions of fibroblasts using atomic force microscopy *Biophys. J.* **86** 1777–93
[33] Azeloglu E U and Costa K D 2011 Atomic force microscopy in mechanobiology: measuring microelastic heterogeneity of living cells *Methods Mol. Biol.* **736** 303–29
[34] Abidine Y, Laurent V M, Michel R, Duperray A and Verdier C 2013 Microrheology of complex systems and living cells using AFM *Comput. Methods Biomech. Biomed. Eng.* **16** 15–6
[35] Haase K and Pelling A E 2015 Investigating cell mechanics with atomic force microscopy *J. R. Soc. Interface* **12** 20140970
[36] Laperrousaz B, Berguiga L, Nicolini F E, Martinez-Torres C, Arneodo A, Maguer-Satta V and Argoul F 2016 Revealing stiffening and brittlening of chronic myelogenous leukemia hematopoietic primary cells through their temporal response to shear stress *Phys. Biol.* **13** 03LT01
[37] Hertz H 1881 About the contact of solid elastic bodies [Über die berührung fester elastischer Körper] *J. Reine Angew. Math.* **92** 156–71
[38] Sneddon I N 1965 The relation between load and penetration in the axisymmetric Boussinesq problem for a punch of arbitrary profile *Int. J. Eng. Sci.* **3** 47–57
[39] Digiuni S, Berne-Dedieu A, Martinez-Torres C, Szecsi J, Bendahmane M, Arneodo A and Argoul F 2015 Single cell wall nonlinear mechanics revealed by a multi-scale analysis of AFM force-indentation curves *Biophys. J.* **108** 2235–48
[40] Savona M and Talpaz M 2008 Getting to the stem of chronic myeloid leukaemia *Nat. Rev. Cancer* **8** 341–50
[41] Jones D 2010 *Neoplastic Hematopathology: Experimental and Clinical Approches* (New York: Humana Press Inc.)
[42] Laperrousaz B, Jeanpierre S, Sagorny K, Voeltzel T, Ramas S, Kaniewski B, Ffrench M, Salesse S, Nicolini F E and Maguer-Satta V 2013 Primitive CML cell expansion relies on abnormal levels of BMPs provided by the niche and BMPRIb overexpression *Blood* **122** 3767–77
[43] McWhirter J R and Wang J Y 1993 An actin-binding function contributes to transformation by the BCR-ABL oncoprotein of Philadelphia chromosome-positive human leukemias *EMBO J.* **12** 1533–46
[44] Cheng K, Kurzrock R, Qiu X, Estrov Z, Ku S, Dulski K M, Wang J Y J and Talpaz M 2002 Reduced focal adhesion kinase and paxillin phosphorylation in BCR-ABL-transfected cells *Cancer* **95** 440–50
[45] Laperrousaz B, Drillon G, Berguiga L, Nicolini F, Audit B, Maguer-Satta V, Arneodo A and Argoul F 2016 From elasticity to inelasticity in cancer cell mechanics: a loss of scale-invariance *AIP Conf. Proc.* **1760** 020040
[46] Ferrer J M, Lee H, Chen J, Pelz B, Nakamura F, Kamm R D and Lang M J 2008 Measuring molecular rupture forces between single actin filaments and actin-binding proteins *Proc. Natl Acad. Sci. USA* **105** 9221–6
[47] Kesten H 1973 Random difference equations and renewal theory for products of random matrices *Acta Math.* **131** 207–48
[48] Mitzenmacher M 2004 A brief history of generative models for power law and lognormal distributions *Internet Math.* **1** 226–51
[49] Malevergne Y, Pisarenko V and Sornette D 2011 Testing the Pareto against the lognormal distributions with the uniformly most powerful unbiased test applied to the distribution of cities *Phys. Rev.* E **83** 036111
[50] Meyers R A (ed) 2009 *Encyclopedia of Complexity and Systems Science* (New York: Springer)
[51] Barabasi A-L and Albert R 1999 Emergence of scaling in random networks *Science* **286** 509–12
[52] Bak P 1996 *How Nature Works: The Science of Self-Organized Criticality* (New York: Springer)
[53] Sornette D 2006 *Critical Phenomena in Natural Sciences. Chaos, Fractals, Self-Organization and Disorder: Concepts and Tools* (*Springer Series in Synergetics*) 2nd edn (Heidelberg: Springer)

[54] Perez-Reche F J, Triguero C, Zanzottto G and Truskinovsky L 2016 Origin of scale-free intermittency in structural first-order phase transitions *Phys. Rev.* B **94** 144102
[55] Mandelbrot B 1982 *The Fractal Geometry of Nature* (New York: Academic)
[56] Arneodo A, Bacry E and Muzy J F 1998 Random cascades on wavelet dyadic trees *J. Math. Phys.* **39** 4142–64
[57] Frisch U 1995 *Turbulence: The Legacy of Kolmogorov* (New York: Cambridge University Press)
[58] Gibrat R 1931 *Les Inégalités Economiques* (Paris: Librairie du 'Recueil Sirey')
[59] Beaulieu N 2012 An extended limit theorem for correlated lognormal sums *IEEE Trans. Commun.* **60** 23–6
[60] Streppa L, Devin A, Schaeffer L, Arneodo A and Argoul F 2018 Prestressed cells are prone to cytoskeleton failures under localized shear strain: an experimental demonstration on muscle precursor cells *Sci. Rep.* accepted (https://doi.org/10.1038/s41598-018-26797-4)
[61] Sharon E and Fineberg J 1996 Microbranching instability and the dynamic fracture of brittle materials *Phys. Rev.* B **54** 7128–39
[62] McWhirter J R and Wang J Y J 1991 Activation of tyrosine kinase and microfilament-binding functions of c-ABL by BCR sequences in BCR-ABL fusion proteins *Mol. Cell. Biol.* **11** 1553–65
[63] Pasternak G, Hochhaus A, Schultheis B and Hehlmann R 1998 Chronic myelogenous leukemia: molecular and cellular aspects *J. Cancer Res. Clin. Oncol.* **124** 643–60
[64] Zhang X and Ren R 1998 BCR-ABL efficiently induces a myeloproliferative disease and production of excess interleukin-3 and granulocyte-macrophage colony-stimulating factor in mice: a novel model for chronic myelogenous leukemia *Blood* **92** 3829–40
[65] Zhao R C, Jiang Y and Verfaillie C M 2001 A model of human p210bcr/ABL-mediated chronic myelogenous leukemia by transduction of primary normal human CD34+ cells with a BCR/ABL-containing retroviral vector *Blood* **97** 2406–12
[66] Clarkson B, Strife A, Wisniewski D, Lambek C L and Liu C 2003 Chronic myelogenous leukemia as a paradigm of early cancer and possible curative strategies *Leukemia* **17** 1211–62
[67] Melo J V and Barnes D J 2007 Chronic myeloid leukaemia as a model of disease evolution in human cancer *Nat. Rev. Cancer* **7** 441–53
[68] Maguer-Satta V, Forissier S, Bartholin L, Martel S, Jeanpierre S, Bachelard E and Rimokh R 2006 A novel role for fibronectin type I domain in the regulation of human hematopoietic cell adhesiveness through binding to follistatin domains of FLRG and follistatin *Exp. Cell. Res.* **312** 434–42
[69] Jeanpierre S, Nicolini F E, Kaniewski B, Dumontet C, Rimokh R, Puisieux A and Maguer-Satta V 2008 BMP4 regulation of human megakaryocytic differentiation is involved in thrombopoietin signaling *Blood* **112** 3154–63
[70] Laperrousaz B 2015 Role of the microenvironment in maintenance and resistance of leukemic stem cells in chronic myelogenous leukemia. BMP pathway and mechanical forces *PhD Thesis* Ecole Normale Supérieure de Lyon
[71] Martinez-Torres C, Berguiga L, Streppa L, Boyer-Provera E, Schaeffer L, Elezgaray J, Arneodo A and Argoul F 2014 Diffraction phase microscopy: retrieving phase contours on living cells with a wavelet-based space-scale analysis *J. Biomed. Opt.* **19** 036007
[72] Martinez-Torres C, Laperrousaz B, Berguiga L, Boyer-Provera E, Elezgaray J, Nicolini F E, Maguer-Satta V, Arneodo A and Argoul F 2015 Deciphering the internal complexity of living cells with quantitative phase microscopy: a multiscale approach *J. Biomed. Opt.* **20** 096005
[73] Martinez-Torres C, Laperrousaz B, Berguiga L, Boyer Provera E, Elezgaray J, Nicolini F E, Maguer-Satta V, Arneodo A and Argoul F 2016 Enlightening intracellular complexity of living cells with quantitative phase microscopy *Proc. SPIE* **9718** 97182C
[74] Kim M-S, Choi J-H, Kim J-H and Park Y-K 2010 Accurate determination of spring constant of atomic force microscope cantilevers and comparison with other methods *Measurement* **43** 520–6
[75] Arneodo A, Vaillant C, Audit B, Argoul F, D'Aubenton-Carafa Y and Thermes C 2011 Multi-scale coding of genomic information: from DNA sequence to genome structure and function *Phys. Rep.* **498** 45–188
[76] Choquet D, Felsenfeld D P and Sheetz M P 1997 Extracellular matrix rigidity causes strengthening of integrin-cytoskeleton linkages *Cell* **88** 39–48
[77] Cappella B and Dietler G 1999 Force–distance curves by atomic force microscopy *Surf. Sci. Rep.* **34** 1–104
[78] Grossmann A and Morlet J 1984 Decomposition of Hardy functions into square integrable wavelets of constant shape *SIAM J. Math. Anal.* **15** 723–36
[79] Meyer Y (ed) 1992 *Wavelets and their Applications* (Berlin: Springer)
[80] Daubechies I 1992 *Ten Lecture on Wavelets* (Philadelphia, PA: Society for Industrial and Applied Mathematics)
[81] Arneodo A, Bacry E and Muzy J 1995 The thermodynamics of fractals revisited with wavelets *Physica* A **213** 232–75
[82] Mallat S 1998 *A Wavelet Tour of Signal Processing* (New York: Academic)
[83] Arneodo A, Audit B, Decoster N, Muzy J F and Vaillant C 2002 Wavelet based multifractal formalism: application to DNA sequences, satellite images of the cloud structure an stock market data *The Science of Disasters: Climate Disruptions, Heart Attacks and Market Crashes* ed A Bunde *et al* (Berlin: Springer) pp 26–102
[84] Arneodo A, Audit B, Kestener P and Roux S 2008 Wavelet-based multifractal analysis *Scholarpedia* **3** 4103
[85] Gabor D 1946 Theory of communication *J. Inst. Electr. Eng.* **93** 429–57
[86] Arneodo A, Grasseau G and Kostelich E J 1987 Fractal dimensions and f(alpha) spectrum of the Henon attractor *Phys. Lett.* A **124** 426–32
[87] Muzy J F, Bacry E and Arneodo A 1993 Multifractal formalism for fractal signals: the structure-function approach versus the wavelet-transform modulus-maxima method *Phys. Rev.* E **47** 875–84
[88] Muzy J F, Bacry E and Arneodo A 1991 Wavelets and multifractal formalism for singular signals: application to turbulence data *Phys. Rev. Lett.* **67** 3515–8
[89] Bacry E, Muzy J F and Arneodo A 1993 Singularity spectrum of fractal signals from wavelet analysis: exact results *J. Stat. Phys.* **70** 635–74
[90] Muzy J F, Bacry E and Arneodo A 1994 The multifractal formalism revisited with wavelets *Int. J. Bifurcation Chaos* **4** 245–302
[91] Delour J, Muzy J F and Arneodo A 2001 Intermittency of 1D velocity spatial profiles in turbulence: a magnitude cumulant analysis *Eur. Phys. J.* B **23** 243–8
[92] Audit B, Bacry E, Muzy J F and Arneodo A 2002 Wavelet-based estimators of scaling behavior *IEEE Trans. Inf. Theory* **48** 2938–54
[93] Ivanov P C, Amaral L A, Goldberger A L, Havlin S, Rosenblum M G, Struzik Z R and Stanley H E 1999 Multifractality in human heartbeat dynamics *Nature* **399** 461–5
[94] Ivanov P C, Nunes Amaral L A, Goldberger A L, Havlin S, Rosenblum M G, Stanley H E and Struzik Z R 2001 From $1/f$ noise to multifractal cascades in heartbeat dynamics *Chaos* **11** 641–52
[95] Goldberger A L, Amaral L A N, Hausdorff J M, Ivanov P C, Peng C K and Stanley H E 2002 Fractal dynamics in physiology: alterations with disease and aging *Proc. Natl Acad. Sci. USA* **99** 2466–72
[96] Arneodo A, Decoster N, Kestener P and Roux S G 2003 A wavelet-based method for multifractal image analysis: from theoretical concepts to experimental applications *Adv. Imaging Electr. Phys.* **126** 1–92

[97] Brianna Caddle L, Grant J L, Szatkiewicz J, Van Hase J, Shirley B J, Bewersdorf J, Cremer C, Arneodo A, Khalil A and Mills K D 2007 Chromosome neighborhood composition determines translocation outcomes after exposure to high-dose radiation in primary cells *Chromosome Res.* **15** 1061–73
[98] Khalil A, Grant J L, Caddle L B, Atzema E, Mills K D and Arneodo A 2007 Chromosome territories have a highly nonspherical morphology and nonrandom positioning *Chromosome Res.* **15** 899–916
[99] Snow C J, Goody M, Kelly M W, Oster E C, Jones R, Khalil A and Henry C A 2008 Time-lapse analysis and mathematical characterization elucidate novel mechanisms underlying muscle morphogenesis *PLoS Genet.* **4** e1000219
[100] Snow C J, Peterson M T, Khalil A and Henry C A 2008 Muscle development is disrupted in zebrafish embryos deficient for fibronectin *Dev. Dyn.* **237** 2542–53
[101] Grant J, Verrill C, Coustham V, Arneodo A, Palladino F, Monier K and Khalil A 2010 Perinuclear distribution of heterochromatin in developing C. elegans embryos *Chromosome Res.* **18** 873–85
[102] Goody M F, Kelly M W, Lessard K N, Khalil A and Henry C A 2010 Nrk2b-mediated {NAD}+ production regulates cell adhesion and is required for muscle morphogenesis *in vivo Dev. Biol.* **344** 809–26
[103] Batchelder K A, Tanenbaum A B, Albert S, Guimond L, Kestener P, Arneodo A and Khalil A 2014 Wavelet-based 3D reconstruction of microcalcification clusters from two mammographic views: new evidence that fractal tumors are malignant and Euclidean tumors are benign *PLoS One* **9** e107580
[104] Gerasimova E, Audit B, Roux S-G, Khalil A, Gileva O, Argoul F, Naimark O and Arneodo A 2014 Wavelet-based multifractal analysis of dynamic infrared thermograms to assist in early breast cancer diagnosis *Frontiers Physiol.* **5** 176
[105] Richard C D, Tanebaum A, Audit B, Arneodo A, Khalil A and Frankel W N 2015 SWDreader: a wavelet-based algorithm using spectral phase to characterize spike-wave morphological variation in genetic models of absence epilepsy *J. Neurosci. Methods* **242** 127–40
[106] Gerasimova-Chechkina E, Toner B, Marin Z, Audit B, Roux S G, Argoul F, Khalil A, Gileva O, Naimark O and Arneodo A 2016 Comparative multifractal analysis of dynamic infrared thermograms and x-ray mammograms enlightens changes in the environment of malignant tumors *Frontiers Physiol.* **7** 336
[107] Marin Z, Batchelder K A, Toner B C, Guimond L, Gerasimova-Chechkina E, Harrow A R, Arneodo A and Khalil A 2017 Mammographic evidence of microenvironment changes in tumorous breasts *Med. Phys.* **44** 1324–36
[108] Martinez-Torres C, Arneodo A, Streppa L, Argoul P and Argoul F 2016 Passive microrheology of soft materials with atomic force microscopy : a wavelet based spectral analysis *Appl. Phys. Lett.* **108** 034102
[109] Roland T, Khalil A, Tanenbaum A, Berguiga L, Delichère P, Bonneviot L, Elezgaray J, Arneodo A and Argoul F 2009 Revisiting the physical processes of vapodeposited thin gold films on chemically modified glass by atomic force and surface plasmon microscopies *Surf. Sci.* **603** 3307–20
[110] Cheng Y-T and Cheng C-M 2004 Scaling, dimensional analysis, and indentation measurements *Mater. Sci. Eng.* R **44** 91–149
[111] Mallat S and Hwang W L 1992 Singularity detection and processing with wavelets *IEEE Trans. Inf. Theory* **38** 617–43